Title

Design and synthesis of multigrain nanocrystals via geometric misfit strain.

Journal

Nature, 577(7790)

ISSN

0028-0836

Authors

Oh, Myoung Hwan
Cho, Min Gee
Chung, Dong Young
et al.

Publication Date

2020

DOI

10.1038/s41586-019-1899-3

Peer reviewed

Design and Synthesis of Multigrain Nanocrystals *via* Geometric Misfit Strain

Authors: Myoung Hwan Oh[1,2,3,4,5,13], Min Gee Cho[1,2,5,13], Dong Young Chung[1,2], Inchul Park[1,6], Youngwook Paul Kwon[7], Colin Ophus[8], Dokyoon Kim[1,2,9], Min Gyu Kim[10], Beomgyun Jeong[11], X. Wendy Gu[12], Jinwoung Jo[1,2], Ji Mun Yoo[1,2], Jaeyoung Hong[1,2], Sara McMains[7], Kisuk Kang[1,6], Yung-Eun Sung[1,2], A. Paul Alivisatos[3,4,5,14]*, and Taeghwan Hyeon[1,2,14]*

Affiliations:

[1]Center for Nanoparticle Research, Institute for Basic Science (IBS), Seoul 08826, Korea.

[2]School of Chemical and Biological Engineering, and Institute of Chemical Processes, Seoul National University, Seoul 08826, Korea.

[3]Department of Chemistry and Department of Materials Science and Engineering, University of California, Berkeley, California 94720, United States.

[4]Materials Sciences Division, Lawrence Berkeley National Laboratory, Berkeley, California 94720, United States.

[5]Kavli Energy NanoScience Institute, University of California, Berkeley, and Lawrence Berkeley National Laboratory, Berkeley, California 94720, United States.

[6]Department of Materials Science and Engineering, Research Institute of Advanced Materials (RIAM), Seoul National University, Seoul 08826, Korea.

[7]Department of Mechanical Engineering, University of California, Berkeley, California 94720, United States.

[8]National Center for Electron Microscopy, Molecular Foundry, Lawrence Berkeley National Laboratory, Berkeley, California, United States.

[9]Department of Bionano Engineering and Bionanotechnology, Hanyang University, Ansan 15588, Korea.

[10]Beamline Research Division, Pohang Accelerator Laboratory, Pohang University of Science and Technology, Pohang 37673, Korea.

[11]Advanced Nano Surface Research Group, Korea Basic Science Institute, Daejeon 34133, Korea.

[12]Department of Mechanical Engineering, Stanford University, Stanford, California 94305, United States.

[13]These authors contributed equally: Myoung Hwan Oh, Min Gee Cho.

[14]These authors jointly supervised this work: A. Paul Alivisatos, Taeghwan Hyeon.

*e-mail: paul.alivisatos@berkeley.edu; thyeon@snu.ac.kr

Summary paragraph

Topological defects associated with grain boundaries (GB defects) have significant effects on the electrical, optical, magnetic, mechanical, and chemical properties of nanocrystalline materials[1,2]. However, elucidating the contribution of specific GB defects to such properties has been a challenging task due to the non-uniformity in grain size and shape, and the random misorientation between the grains[3-5]. Here, we demonstrate that precise control of the heteroepitaxy of colloidal polyhedral nanocrystals enables highly ordered grain growth with defined three-dimensional (3D) symmetry and the production of uniform GB defects, providing an unprecedented opportunity to overcome the limitations of prior sample preparation methods. We synthesized a prototypical multigrain nanocrystal consisting of a Co_3O_4 nanocube core with each facet of the core attached to a Mn_3O_4 shell. The individual shells are symmetry-related interconnected grains[6]. At the sharp edges of the Co_3O_4 nanocubes, the tilt boundaries of these Mn_3O_4 grains join *via* disclinations due to the large geometric misfit between the adjacent tetragonal Mn_3O_4 grains. We set four design principles to produce such highly ordered multigrain nanostructures *via* the geometric misfit strain. First, the shape of the substrate nanocrystal guides the crystallographic orientation of the overgrowth phase[7]. Second, the size of the substrate must be smaller than the characteristic distance between the dislocations. Third, the incompatible symmetry between the overgrowth phase and the substrate increases the geometric misfit between the grains. Finally, under near-equilibrium conditions for the GB formation, the surface energy of the shell is balanced by the increasing elastic energy through ligand passivation[8-10]. Based on these principles, we

produced various combinations of multigrain nanocrystals containing distinct GB defects.

The geometric misfit strain in core/shell nanocrystals was investigated using nanocrystals of polyhedral Co_3O_4 core and heteroepitaxial Mn_3O_4 shell as a model system. We prepared ~11-nm-sized Co_3O_4 nanocubes with {100} facets as a substrate for the growth of Mn_3O_4 (Supplementary Fig. 1a). The formation of Mn_3O_4 grains on the nanocube was carried out by the reaction of $MnCl_2$ or $Mn(HCOO)_2$ in an organic/aqueous (xylene/water) reverse micelle solution in the presence of oleylamine, oleic acid, and HCl[11,12] (Supplementary Methods). X-ray diffraction (XRD) data confirmed that tetragonal Mn_3O_4 (a=b = 5.765 Å, c=9.442 Å, JCPDS #80-0382) was the deposited phase (Supplementary Fig. 1b). It has a spinel structure elongated along the c-axis due to the Jahn–Teller (J–T) effect of Mn^{3+} with an electron configuration of $t_{2g}^3e_g^1$, whereas the Co_3O_4 core has a cubic spinel structure (a=b=c=8.084 Å, JCPDS #42-1467). As shown in Fig. 1a, the lattice of Mn_3O_4 {220} coincides with Co_3O_4 {400} at a misfit of less than 1%, explaining the consistent values in the in-plane interatomic distance (d_{in}) for both phases (Supplementary Figs. 1-3, Supplementary Table 1, Supplementary Methods).

In Fig. 1a, the high-resolution high-angle annular dark-field scanning transmission electron microscope (HAADF-STEM) images and the Fourier-filtered images reveal that for each facet of the cubic core, a Mn_3O_4 grain grows in <001> directions perpendicular to Co_3O_4 {100}, and Mn_3O_4 {110} are parallel to Co_3O_4 {010}. The growth direction of the shell is guided by the lattice matching along six {100} surface planes of the Co_3O_4 core, which leads to the segmentation of the shell into multigrains. An irregularly shaped core induces an inconsistent lattice coincidence, which prevents the formation of an ordered grain structure (Supplementary Figs. 4a-c)[13].

The tetragonal symmetry of Mn_3O_4 produces a gap with an angle of ~8.4° between the {112} planes of adjacent Mn_3O_4 grains along the edges of the Co_3O_4 core[14] (Fig. 1b). Twinned disclinations of Mn_3O_4 {112} with respect to Co_3O_4 {110} are thus formed around the boundary to close the gap. Accordingly, the fast Fourier transform (FFT) of the TEM image with the zone axis along Co_3O_4 [100] shows the extension of the square lattice of Co_3O_4 into Mn_3O_4 (Fig. 1c). A similar FFT analysis with the zone axis along Co_3O_4 [110] further supports the distortion of the Mn_3O_4 lattice structure near the Co_3O_4 nanocube edges (Supplementary Fig. 4d). Each Mn_3O_4 grain has a truncated square pyramidal shape enclosed by {100} and {011} facets (Supplementary Figs. 1c-d). The overall morphology of each Co_3O_4/Mn_3O_4 multigrain nanocrystal can be described as a truncated octahedron consisting of a cubic Co_3O_4 core and Mn_3O_4 grains orthogonally grown from the basal planes of the core.

The overall growth process can be considered to be a generalization or extension of the Stranski-Krastanov (SK) mode growth of a thin film on a two-dimensional (2D) substrate to a finite-sized 3D case. In SK growth, the thin film grows up to a critical layer thickness (h_c), which is determined by the interplay between the strain and the surface energy, followed by 3D island growth[15,16]. From the perspective of extending the SK growth to 3D nanocrystal substrates, as illustrated in Figs. 2a-b, the mechanism by which the grains grow to form the core/shell nanocrystals can be described as follows: The shell initially grows *via* a layer-by-layer mode on the facets of the polyhedral nanocrystal core, forming a coherent layer (CL) and accumulating epitaxial strain (Fig. 2a). When the growth thickness exceeds h_c, the growth mode changes to island growth for strain relaxation. In particular, unless there is a GB that exerts geometric misfit-induced stress (Fig. 1c), the Co_3O_4/Mn_3O_4 core/shell

nanocrystals with the minimal lattice-mismatch exhibit almost no characteristics of CL because the strain energy is so small (Fig. 2c, Supplementary Fig. 2a).

The CLs grown on the facets of the core are differently oriented and meet each other at a certain angle (θ_c) around the sharp edges of the core, forming tilt boundaries (Fig. 2b). Consequently, a geometric strain arises due to the mismatch between the CL lattices rendered by anisotropic strain relaxation of the shell material[17-19]. The mismatch is particularly pronounced in the nanocrystals with an isotropic-lattice-core (i.e., cubic lattice) and anisotropic-lattice-shell (i.e., tetragonal lattice). The h_c of the CL observed for 2D epitaxy is modified in 3D epitaxy to the value at which the geometric misfit strain, in addition to the epitaxial strain, can be accommodated by the shell material. For example, the Mn_3O_4 lattice at the GBs can accommodate the elastic distortion required to create a continuous disclination with a length of three Mn_3O_4 unit cells (~ 2.9 nm; h_c)[20]. Therefore, each Mn_3O_4 shell can be divided into two regions; the '3D geometric CL' with grain boundaries (GBs) and the islands grown further from the CL (Fig. 2b).

When the GB formation is driven energetically, precise management of the kinetic effects during the shell growth is the key to obtain the desired coverage and morphology of the shell grains[21]. In our synthetic method using oleylammonium salts, the acid/base ratio of the solution and the concentration of counteranions can be varied (Supplementary Fig. 5). The deposition rate, a kinetic parameter, and the surface energy of the growing nanocrystals, a thermodynamic parameter, are affected by both the acid/base ratio and the counteranion concentration. The former is more sensitive to the acid/base ratio that controls the supersaturation level, and the latter is responsive to the counteranions bound to the surface. Using this

synthetic system, we can limit the shell growth in a near-equilibrium thin-film growth regime.

By changing the counteranions that passivate the surface of the shell, the morphology of the grains could be controlled to have CLs with (CoMn-CL+I) or without islands (CoMn-CL) (Figs. 2d-e, Supplementary Figs. 5c-e). To compare the stabilizing effects of different types of counteranions, $MnCl_2$ and $Mn(HCOO)_2$ were tested. With $HCOO^-$ ions, lateral growth (i.e., wetting of the core surface) of the grains is promoted without the formation of the islands because the low surface energy can compensate for the energy expended on the epitaxial strain and even the large geometric strain to form the GBs (Fig. 2d). On the other hand, when $MnCl_2$ is used, Mn_3O_4 islands with high surface energy tend to grow on the CLs to relax the strain, and the creation of CLs/GBs is inhibited (Fig. 2e). For almost the same elemental composition, the Mn_3O_4 shell of CoMn-CL has larger coverage, meaning not only more grains and GBs, but also a lower height/edge-length ratio than those of CoMn-CL+I. This behaviour of the shell material, which switches the growth mode between lateral and vertical ones depending on the ligand stabilization capability, minimizes the total free energy while incorporating the geometric misfit strain[9]. To further drive the near-equilibrium growth, we designed the experiments to repeat the shell growth under the same supersaturated conditions (Figs. 2f-g, Supplementary Methods). As a result, the shell coverage increased, and subsequently the GB number also rose, producing the nanocrystals with a near-equilibrium structure in which the grains form a closed loop.

Furthermore, we could tailor the structures of the GB defects (e.g., disclinations and dislocations) either by using different types of counteranions that can promote

non-equilibrium shell growth or changing the core size (Figs. 2h-i, Supplementary Figs. 5f and 6, Supplementary Methods). Because of the stress-relief through the formation of dislocations at the core/shell interface or in the GBs, the GBs were extended along with the periodic/zigzag dislocations.

The structure of the GB defects is illustrated based on the green-squared area in the HAADF-STEM image of the nanocrystal with both GB and island in Supplementary Fig. 7a (Fig. 3a). Here, d_{in} and d_{out} are defined as the interatomic spacings among the M^{2+} cations (M=Co, Mn) that are parallel (in-plane) and perpendicular (out-of-plane) to the interface, respectively, on the 2D projection of the lattice. The d_{out}/d_{in} ratio of 1.03 and the square-like shape of the unit cell at the GB in Fig. 3a result from the rotation of Mn_3O_4 {112} planes around the Mn_3O_4 <220> axes. The FFT of the STEM images of all the CoMn-CL and CoMn-CL+I samples with GBs taken along the Co_3O_4 [100] zone axis consistently show the Bragg reflections of Mn_3O_4 (112) dispersed toward Co_3O_4 (220) reflections (Supplementary Fig. 7).

Strain field mapping was conducted by image-processing the atomic-resolution HAADF-STEM image (Figs. 3b-d, Supplementary Fig. 8, Supplementary Methods). The extent of local distortion was presented in terms of the aspect ratio of the diamond lattice consisting of Co_3O_4 {220} or Mn_3O_4 {112} planes. The colour map images clearly show that the strain field has narrow bands of reduced d_{out}/d_{in} lattices at the GBs around the nanocube edges. The statistical distributions of the aspect ratios were extracted from the white dashed regions that correspond to the lateral views of two adjacent grains sharing a GB. The most common d_{out}/d_{in} values for the nanocrystals with islands are near 1.16, which is close to the $c/\sqrt{2}a$ value of the regular Mn_3O_4 lattice (also see Supplementary Fig. 9). On the other hand, lower

values are observed for the nanocrystals without islands, which can be attributed to the distribution of tensile and compressive strains induced along Mn_3O_4 [220] and [004], respectively, due to the gap closing.

The local strain distribution is reflected in the electron diffraction (ED) patterns and powder XRD data through the reasonably uniform grain configuration in the nanocrystals (Fig. 3e, Supplementary Figs. 9-10). The GB areas and gap angles are almost identical for all the GBs, implying that the residual stresses associated with the gap closing between two grains near each GB are almost the same. At the given residual stress, an island appears to have a less normal strain per plane than a CL according to the strain field mapping. The Mn_3O_4 (112) XRD peak for the CoMn-CL nanocrystals is broader than that for the CoMn-CL+I nanocrystals at a similar Mn content, which indicates a higher proportion of nonuniform deformation due to the smaller volume or the absence of islands. Such uniformity in the GB structure provides a valuable opportunity to investigate the properties of strained GB structures, which are otherwise hard to achieve[5]. For instance, one can obtain the correlation between the microscopic defect structures and the ensemble properties.

When the gap closes, not only is there normal strain and the accompanying Poisson's effect, but also shear strain and rotation of unit cells at the GBs due to the high elastic anisotropy of orthotropic Mn_3O_4[22]. The more accurate strain tensor measurement[23], which is on the scale of 0.5 nm, shows that the normal strain and the rotation are the principal deformation components (Fig. 4, Supplementary Fig. 11, see Supplementary Methods for the algorithm). In both the nanocrystals with and without islands, the aspect ratios of the unit cells at the GBs are close to unity. Furthermore, the sizes of the unit cells increase with increasing distance from the Co_3O_4/Mn_3O_4 interface, and the values are very similar for those at the same distance.

Interestingly, the Mn_3O_4 shell accommodates a large 3D strain (~8% for each axis) per GB without producing any dislocations. The value is quite large compared to Au decahedral nanoparticles, another material well known to exhibit GBs within nanocrystals[14]. Moreover, we demonstrated that the GBs in the form of disclinations could also be created in the core/shell nanocrystals of other material combinations, such as Fe_3O_4/Mn_3O_4, Mn_3O_4/Co_3O_4, Fe_3O_4/Co_3O_4, and Pd/Au, *via* geometric misfit (Supplementary Figs. 12-15, Supplementary Methods).

Thin films in 2D SK growth mode often exhibit periodic ripple patterns along with the island formation, which is mainly attributed to the epitaxial strain[9,24]. Pre-patterned substrates with ordered pit arrays and stripes are used for directing the island growth and ordering[25]. In our demonstration of the 3D analogy of the SK growth, each of the well-defined polyhedral nanocrystals (i.e., core) acts as a pre-patterned substrate. Consequently, a thin-film (i.e., shell) grows with a strain field patterned along the sharp edges due to the geometric misfit strain in addition to the epitaxial strain. This 3D network of strains also organizes the grains into a 3D superlattice[26]. Given that the self-organization of lattice domains in 2D epitaxial thin films has been a key element that brings various new physical phenomena, this utilization of geometric misfit strains in 3D shell growth also facilitates the possibility to further manipulate the properties of nanocrystalline materials for improved applications, such as in mechanics, catalysis, and dielectrics[27-30].

References

1. Siegel, R. W. & Thomas, G. J. Grain boundaries in nanophase materials. *Ultramicroscopy* **40**, 376–384 (1992).
2. Ovid'ko, I. A. Deformation of nanostructures. *Science* **295**, 2386 (2002).
3. Read, W. T. & Shockley, W. Dislocation models of crystal grain boundaries. *Phys. Rev.* **78**, 275–289 (1950).
4. Liu, H. H. *et al.* Three-dimensional orientation mapping in the transmission electron microscope. *Science* **332**, 833–834 (2011).
5. Feng, B. *et al.* Atomic structures and oxygen dynamics of CeO_2 grain boundaries. *Sci. Rep.* **6**, 20288 (2016).
6. Lu, K. Stabilizing nanostructures in metals using grain and twin boundary architectures. *Nat. Rev. Mater.* **1**, 16019 (2016).
7. Klapper, H. & Rudolph, P. in *Handbook of Crystal Growth 2* 1093–1141 (Elsevier, 2015).
8. Kwon, S. G. *et al*. Heterogeneous nucleation and shape transformation of multicomponent metallic nanostructures. *Nat. Mater.* **14**, 215–223 (2015).
9. Dixit, G. K. & Ranganathan, M. Consequences of elastic anisotropy in patterned substrate heteroepitaxy. *Nanotechnology* **29**, 365305 (2018).
10. Yang, B., Liu, F. & Lagally, M. G. Local strain-mediated chemical potential control of quantum dot self-organization in heteroepitaxy. *Phys. Rev. Lett.* **92**, 025502 (2004).
11. Oh, M. H. *et al*. Galvanic replacement reactions in metal oxide nanocrystals. *Science* **340**, 964–968 (2013).
12. Pan, A. *et al.* Insight into the ligand-mediated synthesis of colloidal $CsPbBr_3$ perovskite nanocrystals: The role of organic acid, base, and cesium precursors. *ACS Nano* **10**, 7943–7954 (2016).
13. Tsivion, D., Schvartzman, M., Popovitz-Biro, R., von Huth, P. & Joselevich, E. Guided growth of millimeter-long horizontal nanowires with controlled orientations. *Science* **333**, 1003–1007 (2011).
14. Johnson, C. L. *et al*. Effects of elastic anisotropy on strain distributions in decahedral gold nanoparticles. *Nat. Mater.* **7**, 120–124 (2008).
15. Shklyaev, O. E., Beck, M. J., Asta, M., Miksis, M. J. & Voorhees, P. W. Role of strain-dependent surface energies in Ge/Si(100) island formation. *Phys. Rev. Lett.* **94**, 176102 (2005).

16. Chen, G. *et al.* Formation of Ge nanoripples on vicinal Si (1110): From Stranski-Krastanow seeds to a perfectly faceted wetting layer. *Phys. Rev. Lett.* **108**, 055503 (2012).

17. Sneed, B. T., Young, A. P. & Tsung, C.-K. Building up strain in colloidal metal nanoparticle catalysts. *Nanoscale* **7**, 12248–12265 (2015).

18. Foster, C. M., Pompe, W., Daykin, A. C. & Speck, J. S. Relative coherency strain and phase transformation history in epitaxial ferroelectric thin films. *J. Appl. Phys.* **79**, 1405–1415 (1996).

19. Sun, Y. *et al.* Ambient-stable tetragonal phase in silver nanostructures. *Nat. Commun.* **3**, 971–976 (2012).

20. Romanov, A. E. & Kolesnikova, A. L. Application of disclination concept to solid structures. *Prog. Mater. Sci*. **54**, 740–769 (2009).

21. Gránásy, L., Podmaniczky, F., Tóth, G. I., Tegze, G. & Pusztai, T. Heterogeneous nucleation of/on nanoparticles: A density functional study using the phase-field crystal model. *Chem. Soc. Rev.* **43**, 2159–2173 (2014).

22. Gaillac, R., Pullumbi, P. & Coudert, F. X. ELATE: An open-source online application for analysis and visualization of elastic tensors. *J. Phys. Condens. Matter* **28**, 275201–275205 (2016). (URL: http://progs.coudert.name/elate/mp?query=mp-18759)

23. Ophus, C., Ciston, J. & Nelson, C. T. Correcting nonlinear drift distortion of scanning probe and scanning transmission electron microscopies from image pairs with orthogonal scan directions. *Ultramicroscopy* **162**, 1–9 (2016).

24. Hu, H., Gao, H. J. & Liu, F. Theory of directed nucleation of strained islands on patterned substrates. *Phys. Rev. Lett.* **101**, 216102 (2008).

25. Zhong, Z. & Bauer, G. Site-controlled and size-homogeneous Ge islands on prepatterned Si (001) substrates. *Appl. Phys. Lett.* **84**, 1922–1924 (2004).

26. Damodaran, A. R. *et al.* New modalities of strain-control of ferroelectric thin films. *J. Phys.: Condens. Matter* **28**, 263001 (2016).

27. Li, X., Wei, Y., Lu, L., Lu, K. & Gao, H. Dislocation nucleation governed softening and maximum strength in nano-twinned metals. *Nature* **464**, 877–880 (2010).

28. Mariano, R. G., Mckelvey, K., White, H. S. & Kanan, M. W. Selective increase in CO_2 electroreduction activity at grain-boundary surface terminations. *Science* **358**, 1187–1192 (2017).

29. Fan, F. *et al*. Continuous-wave lasing in colloidal quantum dot solids enabled by facet-selective epitaxy. *Nature* **544**, 75–79 (2017).

30. Gao, P. *et al.* Atomic-scale mechanisms of ferroelastic domain-wall-mediated ferroelectric switching. *Nat. Commun.* **4**, 2791 (2013).

Figures and Legends

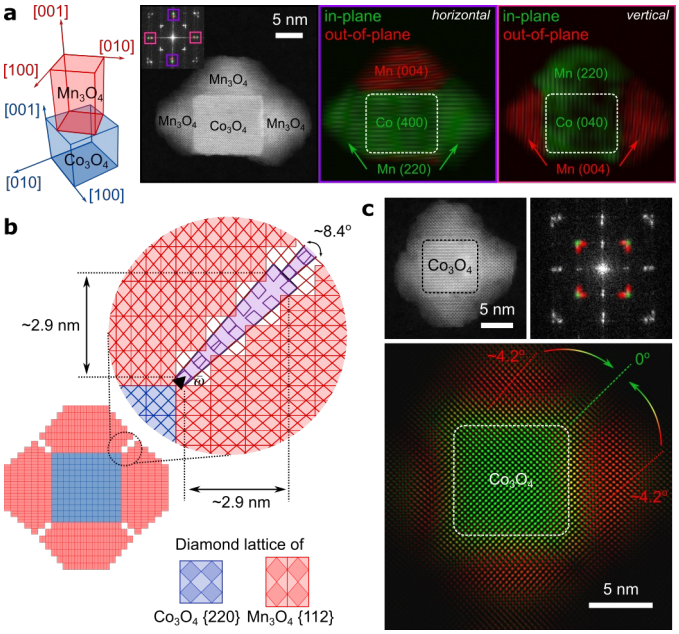

Figure 1. Epitaxially guided growth and gap closing of Mn_3O_4 grains on a Co_3O_4 nanocube. a, Illustration of the orientation relationship between Mn_3O_4 and Co_3O_4 unit cells. HAADF-STEM image and corresponding FFT of the Co_3O_4/Mn_3O_4 nanocrystal taken along the Co_3O_4 <100> and Mn_3O_4 <110> zone axes that shows the orientation relationship between the Co_3O_4 core and Mn_3O_4 grains. The in-plane (outer) spots in the FFT pattern are mapped in green (2.04 Å) and the out-of-plane (inner) spots are mapped in red (2.36 Å). **b,** Illustration of the gaps between adjacent Mn_3O_4 grains resulting in disclinations at the Mn_3O_4 GBs. The misorientation angle between the neighbouring Mn_3O_4 {112} is ~8.4°. The disclination line is designated as a black triangle with Frank vector, ⃗. **c**, The GBs observed in the HAADF-STEM image and a corresponding lattice spacing map. The green and red spots in the FFT image were used to visualize the lattice spacing distribution in the nanocrystal. In the map, the interface between the Co_3O_4 nanocrystal and the Mn_3O_4 GBs is mapped as green, showing that the lattice spacing at the interface is 2.85 Å (Lattice spacings of the Mn_3O_4 {112} planes not affected by the Co_3O_4 core range from 2.96 to 3.09 Å (red)).

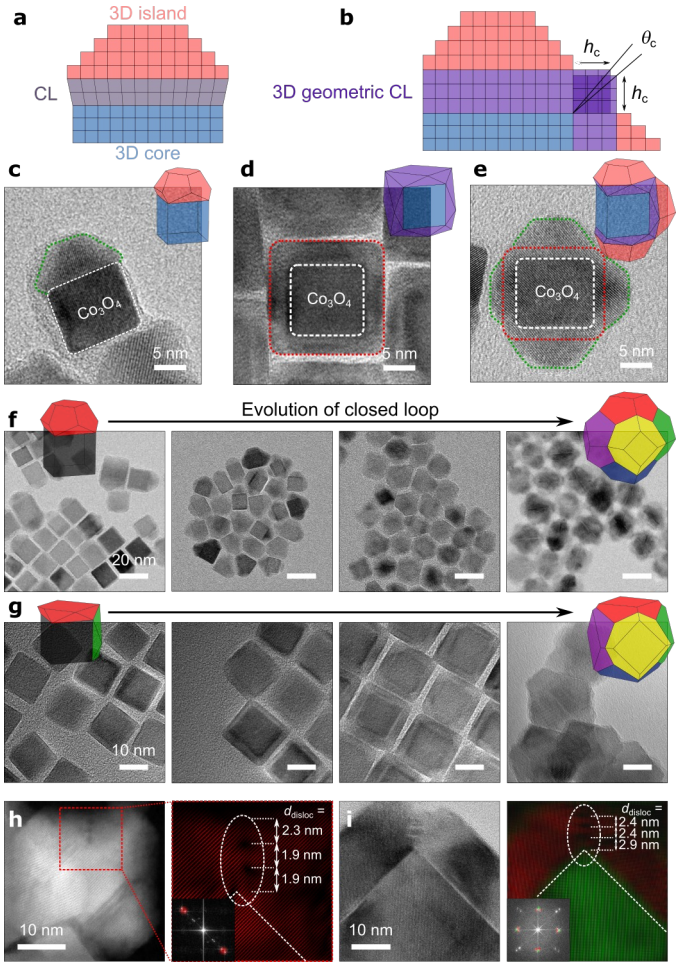

Figure 2. Extension of SK growth to 3D polyhedral substrates. a-b, Schematic illustration of traditional SK growth without geometric misfit strain (**a**) and extended SK growth with '3D geometric CL' induced by geometric misfit strain along the sharp edges of the core (**b**). **c**, TEM image of a Co_3O_4/Mn_3O_4 nanocrystal without GB. **d-e**, TEM images showing the effects of the counteranions in manganese (II) precursors on the morphology of Mn_3O_4 grains without island (**d**) and with island (**e**). Red and green lines in the high-resolution TEM images indicate the CL and the islands of Mn_3O_4, respectively. **f-g,** The development of grains and GBs monitored while repeating the synthetic procedure using chloride (**f**) and formate (**g**) ligands with 11 nm-sized core. **h-i,** STEM, TEM, and FFT images of Co_3O_4/Mn_3O_4 nanocrystals synthesized using 11 nm (**h**) and 30 nm-sized (**i**) Co_3O_4 nanocubes as cores and having GBs longer than a critical thickness. The FFT images show the induced dislocation and its spacing at the Mn_3O_4 GB.

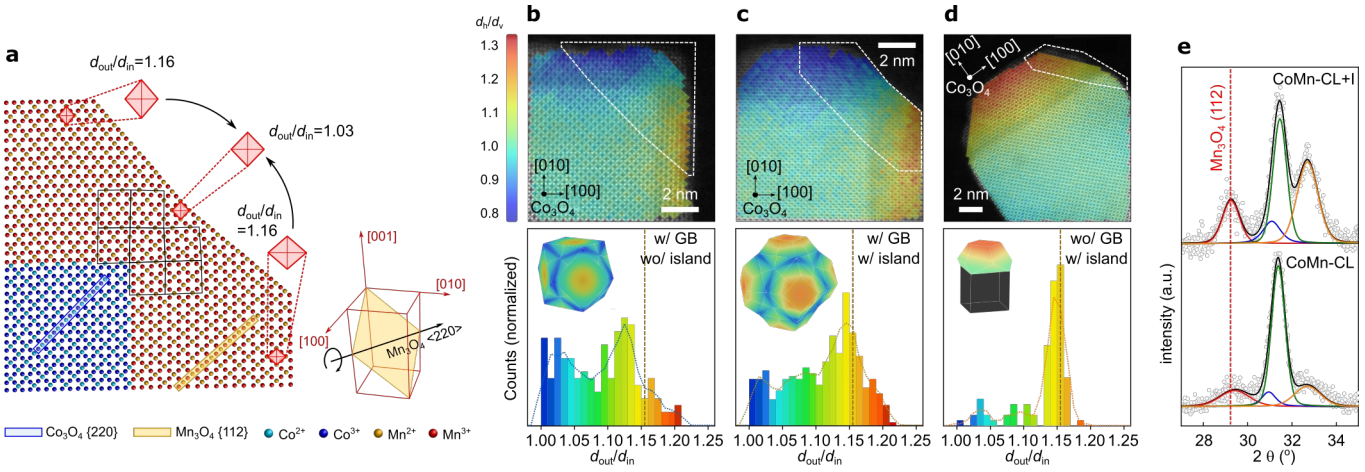
a
d_{out}/d_{in}=1.16
d_{out}/d_{in}=1.03
d_{out}/d_{in} =1.16
[001]
[010]
[100]
Mn_3O_4 <220>
Co_3O_4 {220}
Mn_3O_4 {112}
Co^{2+}
Co^{3+}
Mn^{2+}
Mn^{3+}
d_h/d_v
1.3
1.2
1.1
1.0
0.9
0.8
b
c
d
2 nm
[010]
[100]
Co_3O_4
w/ GB
wo/ island
w/ GB
w/ island
wo/ GB
w/ island
Counts (normalized)
1.00 1.05 1.10 1.15 1.20 1.25
d_{out}/d_{in}
e
Mn_3O_4 (112)
CoMn-CL+I
CoMn-CL
intensity (a.u.)
28 30 32 34
2 θ (°)

Figure 3. GB defects in Co_3O_4/Mn_3O_4 nanocrystals. a, 2D illustration of the atomic arrangement of the nanocrystal with both GB and island. Black rectangles represent the distorted Mn_3O_4 unit cells viewed along the [110] direction. Mn_3O_4 {112} planes rotate around <220>. **b-d**, Computer-vision based image processing results for the diamond lattices consisting of Co_3O_4 {220} or Mn_3O_4 {112} planes and histograms for the aspect ratio distribution of the diamond lattices in the white-lined regions of the nanocrystals with GB/without island (**b**), with both GB and island (**c**), and without GB/with island (**d**). Coloured maps show the distribution of strained diamond lattice cells. In the maps, the horizontal length (d_h) of the lattice cells is divided by the vertical length (d_v) to distinguish the orientations of the grains. In the histogram, ratios greater than 1 are used to obtain the d_{out}/d_{in} values, i.e. the larger of d_h/d_v and d_v/d_h. The insets show 3D models illustrating the strain field of the Mn_3O_4 grains. Vertical dotted lines represent the aspect ratio (1.16) of unstrained Mn_3O_4. **e**, XRD patterns and calculated peak profiles of Co_3O_4/Mn_3O_4 nanocrystals with GBs. Individual peak profiles are Mn_3O_4 (112) (red), (020) (blue), (013) (orange), and Co_3O_4 (220) (green). FWHM of Mn_3O_4 (112) peak increases significantly from 0.90° for CoMn-CL+I to 1.56° for CoMn-CL.

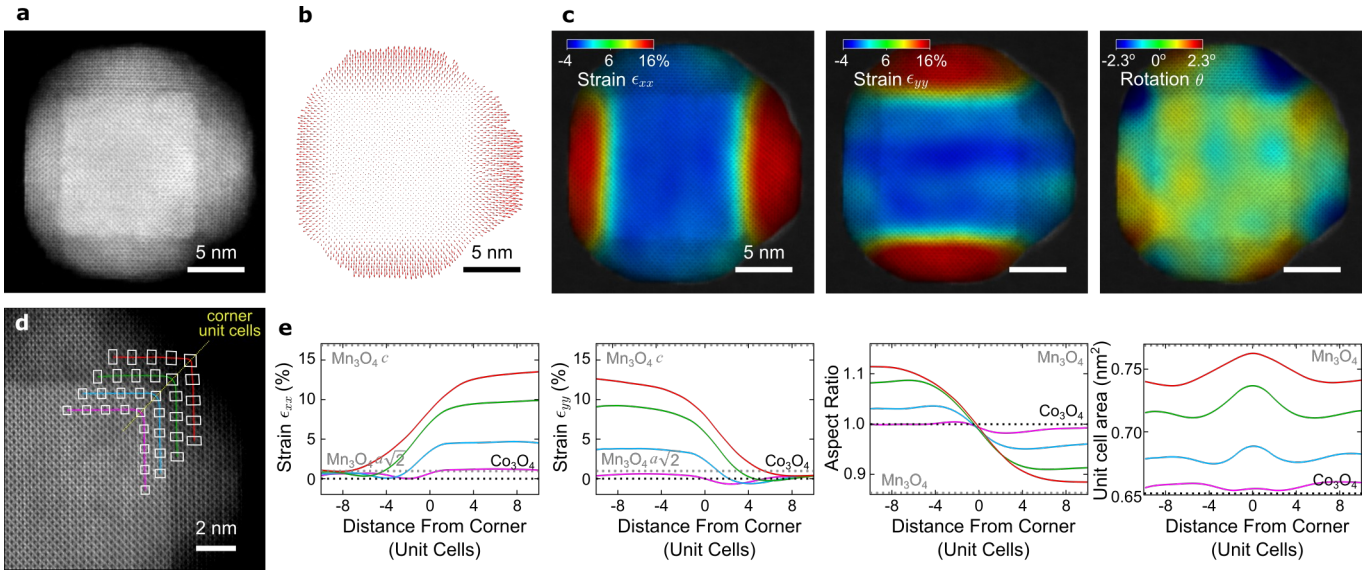

Figure 4. Strain tensor measurements of Co_3O_4/Mn_3O_4 nanocrystal. a, HAADF-STEM image of the nanocrystal. **b**, A map of displacement based on the atomic position of Co_3O_4. **c**, Infinitesimal strains and rotation for *x* and *y* directions and rotation of the unit cell. **d**, Line traces (coloured lines) and unit cells (white rectangles) showing the change in aspect ratio and volume of the unit cells. **e**, The infinitesimal strains for *x* and *y* directions, aspect ratio, and unit cell area over the line traces shown in (**d**).

Acknowledgments: Synthesis and image analysis of the nanocrystal samples were supported by the Research Center Program of the IBS (IBS-R006-D1) in Korea (T.H.) and IBS (IBS-R006-G1) in Korea (Y.–E.S. and K.K.); The theoretical aspects of this work were also supported by the U.S. Department of Energy, Office of Science, Office of Basic Energy Sciences, Materials Sciences and Engineering Division, under Contract No. DE-AC02-05-CH11231 within the Physical Chemistry of Inorganic Nanostructures Program (KC3103) (A.P.A.). Computational work was supported by the Supercomputing Center/Korea Institute of Science and Technology Information with supercomputing resources including technical support (KSC-2014-C3-037) (K.K.). Work at the Molecular Foundry was supported by the Office of Science, Office of Basic Energy Sciences, of the U.S. Department of Energy under Contract No. DE-AC02-05CH11231. Experiments at PLS-II were supported in part by MSIP and POSTECH.

Author Contributions: M.H.O., M.G.C., A.P.A., and T.H. conceived the research. M.H.O. and M.G.C. designed and performed the experiments, and analyzed the results. I.P. and K.K. performed the DFT calculations and analysis. Y.P.K. and S.M. conducted the computer-vision based image processing of HAADF-STEM images. C.O. conducted the strain tensor measurements for the HAADF-STEM micrographs. M.G.K. and B.J. contributed to the analysis of XAS and XPS data, respectively. D.Y.C., J.M.Y., D.K., X.W.G, and Y.-E.S. discussed and commented on the results. J.J. and J.H. prepared the samples for the TEM analysis. M.H.O., M.G.C., D.K., A.P.A., and T.H. wrote the manuscript. A.P.A. and T.H. supervised the project. All the authors commented on the manuscript.

Competing interests: The authors declare no competing interests.

Additional information.

Supplementary information is available for this paper.

Reprints and permissions information is available at http://www.nature.com/reprints.

Correspondence and requests for materials should be addressed to A.P.A or T.H.

Data availability. The data that produce and support the findings of this study are available from the corresponding author upon request.

Code availability. Strain and rotation mapping using real-space peak fitting, geometric phase analysis, and other Fourier filtering measurements were performed using custom MATLAB scripts. The raw image data and analysis codes are freely available upon reasonable request.